ELSEVIER

Comput. Methods Appl. Mech. Engrg. 191 (2001) 73–92

Computer methods in applied mechanics and engineering

www.elsevier.com/locate/cma

Dynamic shear band propagation and micro-structure of adiabatic shear band

Shaofan Li [a], Wing-Kam Liu [b,*], Dong Qian [b], Pradeep R. Guduru [c], Ares J. Rosakis [c]

[a] *Department of Civil and Environmental Engineering, University of California, Berkeley, CA 94720, USA*
[b] *Department of Mechanical Engineering, The Technological Institute, Northwestern University, 2145 Sheridan Road, Evanston, IL 60208-3111, USA*
[c] *Graduate Aeronautical Laboratories, California Institute of Technology, Pasadena, CA 91125, USA*

Received 23 November 2000; received in revised form 16 February 2001

Abstract

Meshfree Galerkin approximations in both two and three dimensions have been used in simulations of dynamic shear band propagation in an asymmetrically impact-loaded prenotched plate. Failure mode switching and failure mode transitions, which have been reported experimentally, are replicated in numerical computations. For intermediate impact speed (25 m/s $< V \leqslant$ 30 m/s), the numerical results show that a cleavage crack initiates from the tip of the dynamic shear band, indicating a dominance of brittle failure mode, and a failure mode switch (ductile-to-brittle: shearband-to-crack). For high impact velocities ($V >$ 30 m/s), the numerical results show that a dynamic shear band penetrates through the specimen without trace of cleavage-type fracture, which is a ductile failure mode. Overall, with the increase of impact speed, the final failure mode of the impacted plate transits from brittle failure to ductile failure. By introducing a multi-physics model to describe the stress collapse state of the shear band, it has been found that there is a non-uniform temperature distribution inside the adiabatic shear band. Strong evidences indicate that temperature distribution inside the shear band has periodic patterns in both space and time, confirming the latest experimental results of P. Guduru et al. [Mech. Mater. (2000), submitted]. This suggests that there may exist a thermal–mechanical instability within the adiabatic shear band, reminiscent of hydrodynamic instability due to viscous heating.

Keywords: Adiabatic shear band; Dynamic shear band propagation; Crack propagation; Failure mode transition; Meshfree methods; Strain localization; Multi-physics modeling

1. Introduction

One of the important achievements of experimental mechanics in the late 20th century is the optical/infrared diagnostics and measurement of dynamic shear band propagation. Although the physical phenomenon may have been known for at least two decades or more, the precise observation and measurement of such physical process had not been obtained until the late 1980s. The pioneer work conducted by Kalthoff and Winkler [15,18,16] (here it is referred to as KW problem in the rest of paper) and the equally important work conducted by Marchand and Duffy [32] led to active studies of dynamic shear band propagation and failure mode transition during recent years (relevant references may be found in a special issue of *International Journal of Fracture*, Vol. 101, 2000).

* Corresponding author. Tel.: +847-491-7094; fax: +847-491-3915.
E-mail addresses: li@ce.berkeley.edu (S. Li), w-liu@northwestern.edu (W.-K. Liu), d-qian@northwestern.edu (D. Qian), pradeep@its.caltech.edu (P.R. Guduru), rosakis@aero.caltech.edu (A.J. Rosakis).

0045-7825/01/$ - see front matter
PII: S0045-7825(01)00245-6

Several authors have conducted similar experiments under different designs and different experiment settings, notably Mason et al. [33] and Zhou et al. [51,52] (here it is referred to as ZRR problem in the rest of paper). They have used a single notch specimen in an impact test to observe dynamic shear band propagation, in contrast to the double notch impact plate experiment conducted by Kalthoff and Winkler [18]. Ravi-Chandar [42] also carried out a similar experiment on polycarbonate plate impact test. Remarkably, all the experiments unequivocally support an unusual fact that under high strain rate condition, there is a "brittle-to-ductile" failure mode transition. When impact velocity in an intermediate range $V_{TF} < V \leqslant V_{SB}$ (subscript "TF" denotes tension fracture, and subscript "SB" denotes shear band) [15], a local mode-I crack is initiated from the notch tip and propagates in a direction upward from the notch line direction (70° in [15,18] and 30° in [52]). The subtlety between the KW problem and the ZRR problem is that at intermediate impact speed range the KW experiment shows the mode-I crack directly initiated from the notch tip, whereas in the ZRR experiment a shear band is first initiated from crack tip and subsequently a mode-I crack is initiated from the shear band tip (the so-called failure mode switch: ductile-to-brittle). In both events, the final failure mode is a brittle failure in this impact speed range. When bullet impact velocity exceeds a threshold limit, V_{SB}, all the experimental results reported that a shear band is intiated from the notch tip, and propagates through the thin plate specimen without trace of cleavage fracture, i.e. the final failure mode is a purely ductile failure. This change of final failure mode with the increase of the impact speed has been referred to as the dynamic failure mode transition, as Kalthoff puts, "*the higher the loading rate in mode-II tests, the harder it is to fulfill the requirement of sufficiently large in-plane dimensions and, consequently, the most favorable become the conditions for a non-linear ductile type failure of the material as represented by shear band failure mechanisms*" (from [17]).

However, theoretical analyses as well as numerical simulations failed to predict such experimental outcome, and in general, dynamic shear band propagation has remained to be elusive to numerical simulations. The few published simulation results [1,2,38,39] have not been able to capture the physical process of dynamic shear band propagation. The simulation reported by Zhou et al. [51] is the only successful numerical simulation in observing dynamic shear band propagation, but it also failed to predict failure mode transition. Recently, by using a meshfree Galerkin method, Li et al. [25] successfully replicated dynamic shear band propagation in a single notched plate (ZRR problem), and observed the failure mode transition for the first time in numerical simulations.

Several technical issues have arisen in numerical simulations of dynamic shear band propagation. First, it has not been clear on how to model the stress collapsing state of a shear band. Without proper modeling of stress collapsing state of the shear band, the widely spread, phenomenological, thermo-elastic–viscoplastic constitutive models seem to be incapable of providing the sufficient information to describe post-bifurcation behaviors of strain localization zone. In order to simulate dynamic shear band propagation, a multiple physics mode may be needed in constitutive modeling of dynamic shear band. This opinion has gained some ground in recent years [2,51], because no one has yet found propagations of a weakly singular surface (localization zone) in numerical simulations based on conventional approach. Zhou et al. [51] adopted a Newtonian fluid for constitutive modeling of a 2D shear band (plane strain), whereas Batra and Nechitailo [2] used a compressible ideal fluid to model the 2D shear band in the localization zone. This multiple constitutive law approach has made it possible to simulate dynamic shear band growth. Nevertheless, its foundation has not been fully justified yet, and it introduces new problems: the presence of small viscous force will cause severe mesh distortion due to large plastic flow motions in Lagrangian type of finite element implementation. Furthermore, strong mesh-alignment sensitivity of finite element methods contributes another source for the inability of conventional numerical methods to simulate such physical processes.

A very suitable computational paradigm for shear band simulations is the meshfree Galerkin method [21,25], a state-of-the-art technology in computational mechanics [4,22,27–31,36]. In this work, a 3D meshfree Galerkin simulation of dynamic shear band propagation is presented, which faithfully replicates the entire process of the failure mode transition at various impact speeds. Different from our early computations [25], the impact event is modeled as a rigid projectile colliding with a single pre-notched plate, whereas in our previous computation [25] prescribed velocity boundary condition is imposed at the impact zone to mimic collision conditions. The other important aspect of this study is to justify the use of

multi-physics constitutive laws in modeling dynamic shear band formation. By choosing the suitable multi-physics model, we have studied the micro-structure of adiabatic shear band. It has been found that the temperature field, effective stress, as well as effective strain fields within the strain localization zone are dynamically structured, which confirms the recent experimental measurement made by Guduru et al. [14]. They have reported that there is a periodic distribution of "hot spots" in temperature profile within the shear band. It appeared that there is thermo-mechanical instability within the adiabatic shear band, which causes periodic temperature distribution in space as well as in time.

2. Formulations

2.1. An explicit meshfree Galerkin formulation

Recently, meshfree methods have been successfully used in simulations of strain localization problems [20,21,23,24]. It has been shown that meshfree method, in particular the reproducing kernel particle method [26,28–30], has a natural ability to avoid mesh-alignment sensitivity that finite element methods have long suffered, mesh distortion under large deformation, as well as volumetric locking for incompressible materials. Therefore, it is a natural choice to use meshfree method to undertake this task.

The basic idea of the reproducing kernel particle method (RKPM) is to construct a proper kernel function on a set of randomly distributed particles ((1) there is no mesh here! (2) the word randomly implies the particle distribution is also statistically isotropic). By doing so, one may approximate a function desired through a "reproducing" or "filtering" representation

$$u_\varrho(x) = \mathscr{R}_\varrho u(x) = \int_\Omega \mathscr{K}_\varrho(y-x)u(y)\mathrm{d}\Omega, \tag{1}$$

where $\mathscr{K}_\varrho(X) := 1/\varrho^n \mathscr{K}(X/\varrho)$, ρ is the dilation parameter that is associated with the support size of the kernel function, and n is the spatial dimension. The RKPM kernel function is compact supported, and usually very smooth, $\mathscr{K}(X) \in C^N(\Omega)$ and $N > 1$. The 3D tri-linear RKPM meshfree shape function used in computations is constructed by using the following polynomial basis:

$$\mathbf{P}(X) = \{1, X_1, X_2, X_3, X_1X_2, X_2X_3, X_3X_1, X_1X_2X_3\}, \tag{2}$$

where $X := (X_1, X_2, X_3)$. Embedding either a cubic spline box function, or a fifth-order spline box function as window function, the kernel function can be explicitly written as

$$\mathscr{K}_\ell(X) = \mathscr{K}_\rho(X_\ell - X) := \mathbf{P}\left(\frac{X_\ell - X}{\varrho}\right)\mathbf{b}(X)\phi_\varrho(X_\ell - X)\Delta V_\ell, \tag{3}$$

where $\phi_\varrho(X)$ is the normalized window function, ΔV_ℓ is the integration weight, and the vector $\mathbf{b}(X)$ is determined by solving the following algebraic equation:

$$\mathbf{M}(X)\mathbf{b}(X) = \mathbf{P}(0), \quad \text{where } \mathbf{P}(0) = \{1, 0, \ldots, 0, 0\}^{\mathrm{T}}, \tag{4}$$

where the moment matrix

$$\mathbf{M}(X) = \sum_{I=1}^{NP} \mathbf{P}^{\mathrm{T}}\left(\frac{X_I - X}{\rho}\right)\mathbf{P}\left(\frac{X_I - X}{\rho}\right)\Delta V_I.$$

After all the laboring, the reproducing kernel particle interpolation can be put into a simple form

$$u_i^\rho(X) = \sum_{I \in \Lambda} \mathscr{K}_I(X)u_{iI}, \quad i = 1, 2, 3. \tag{5}$$

To visualize the spatial profile of such a shape function, we plot a single shape function and its three first-order derivatives in Fig. 1. Even though the support size of the shape function is a rectangular box, one may

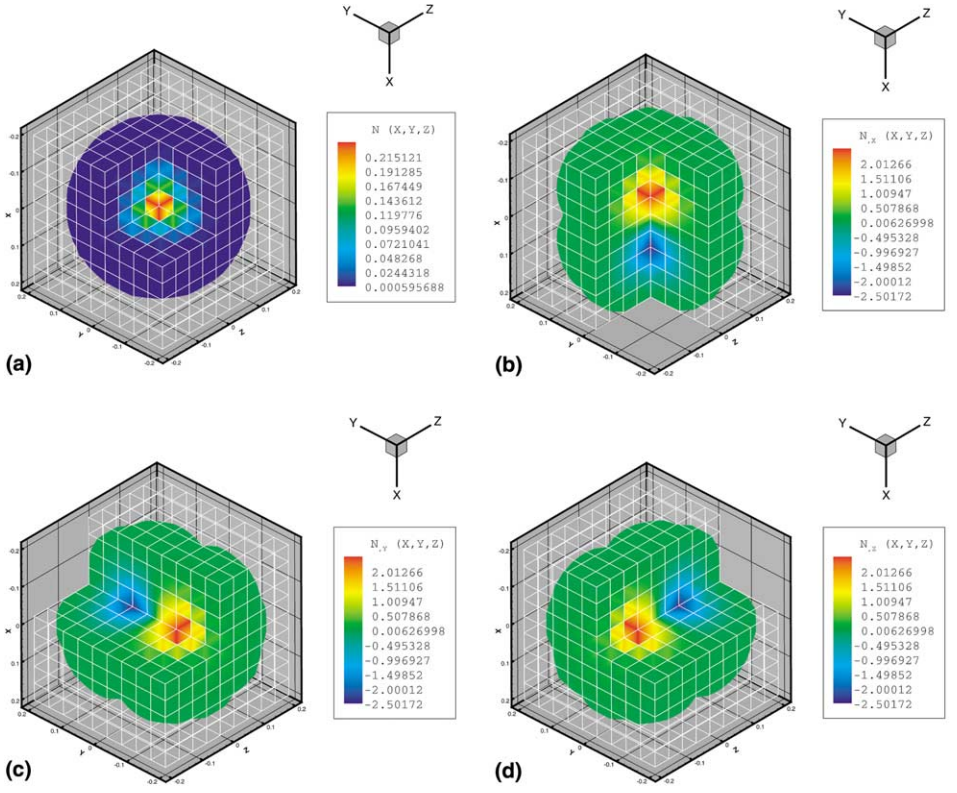

Fig. 1. 3D RKPM/meshfree shape function and its first derivatives generated by the tri-linear polynomial basis, $\mathbf{P}(X) = (1, X_1, X_2, X_3, X_1X_2, X_2X_3, X_3X_1, X_1X_2X_3)$: (a) the shape function, $\mathscr{K}_I(X)$; (b) the derivative, $\mathscr{K}_{I,X_1}(X)$; (c) the derivative, $\mathscr{K}_{I,X_2}(X)$; (d) the derivative, $\mathscr{K}_{I,X_3}(X)$.

observe from Fig. 1 that the domain of non-zero value of the shape function tends to be a sphere, and the domain of non-zero value of the derivatives of the shape function are two connected spherical regions; this means that the spatial distribution of RKPM shape function is almost "isotropic", which is a desired property in some situations, such as shear band simulation. In Fig. 1(a), we take the first octant out from the quasi-sphere region, and one can see that the shape function reaches its maximum at the corresponding particle, i.e. the center. In each of Fig. 1(b)–(d), we take one quadrant out to see the orientation and the distribution of the derivatives.

Note that an RKPM representation is a spatial convolution in a strict sense, whereas the finite element interpolation can be viewed as a spatial convolution only in the sense that the kernel function is a generalized function. Assume that in the domain Ω there is a valid particle distribution, $\Lambda := \{1, 2, \ldots, \ldots, NP\}$. Discretizing (1) yields

$$u^h(X) = \sum_{I=\Lambda} \mathscr{K}_\varrho(X_I - X)\Delta V_I u_I. \tag{6}$$

Eq. (6) represents a special interpolation, which is related with discrete convolution. For simplicity, in the rest of the paper, we shall simply denote $\mathscr{K}_\varrho(X_I - X)\Delta V_I$ as $N_I(X)$. Eq. (6) can be viewed as a non-local interpolation (or not a "interpolation" based on the conventional definition). In such "non-local interpolation", any points in the domain, including particle points, are covered by multiple shape functions (note that in finite element approximation, the nodal point is only covered by a single shape function).

Let $\mathbf{x}$ denote the spatial location of a material point and $\mathbf{X}$ denote the referential location of this material point, the displacement of the material point is defined as

$$\mathbf{u} := \mathbf{x} - \mathbf{X}. \tag{7}$$

The deformation gradient is given by

$$\mathbf{F} := \frac{\partial \mathbf{x}}{\partial \mathbf{X}}. \tag{8}$$

A weak form of the balance of linear momentum can be written as

$$\int_{\Omega_0} \mathbf{P} : \delta \mathbf{F}^{\mathrm{T}} \, \mathrm{d}\Omega_0 = \int_{\Omega_0} \rho_0 \mathbf{B} \cdot \delta \mathbf{u} \, \mathrm{d}\Omega_0 + \int_{\Gamma_0^{\mathrm{T}}} \mathbf{T} \cdot \delta \mathbf{u} \, \mathrm{d}\Gamma_0 - \int_{\Omega_0} \rho_0 \frac{\partial^2 \mathbf{u}}{\partial t^2} \delta \mathbf{u} \, \mathrm{d}\Omega_0, \tag{9}$$

where $\mathbf{T}$ is the prescribed traction on the traction boundary, $\mathbf{B}$ is the body force, Γ_0^{T}, and $\mathbf{P}$ denotes the nominal stress tensor, which can be related to the Kirchhoff stress tensor as $\boldsymbol{\tau} = \mathbf{F} \cdot \mathbf{P}$. For simplicity, the boundary conditions are specified with respect to the referential configuration

$$\mathbf{n}_0 \cdot \mathbf{P} = \mathbf{T} \quad \forall \mathbf{X} \in \Gamma_0^{\mathrm{T}}, \tag{10}$$

$$\mathbf{u} = \bar{\mathbf{u}} \quad \forall \mathbf{X} \in \Gamma_0^{u}, \tag{11}$$

where $\Gamma_0^{\mathrm{T}} \cup \Gamma_0^{u} = \partial\Omega_0$.

Assume that the trial, and weighting functions have the forms

$$\mathbf{u}^h(\mathbf{X}, t) = \sum_{I=1}^{NP} N_I(\mathbf{X}) \mathbf{d}_I(t), \tag{12}$$

$$\delta \mathbf{u}^h(\mathbf{X}, t) = \sum_{I=1}^{NP} N_I(\mathbf{X}) \delta \mathbf{d}_I(t), \tag{13}$$

where NP is the total number of particles.

The weak form (9) will yield the following discrete equations:

$$\mathbf{M} \frac{\mathrm{d}^2 \mathbf{u}^h}{\mathrm{d}t^2} = \mathbf{f}^{\mathrm{ext}} - \mathbf{f}^{\mathrm{int}}. \tag{14}$$

The conventional row-sum lumped technique is adopted in computing mass matrix, $\mathbf{M}$, and the external and internal forces are calculated as follows:

$$\mathbf{f}_I^{\mathrm{ext}} = \int_{\Gamma^{\mathrm{T}}} T_i^h(\mathbf{X}, t) N_I \mathbf{e}_i \, \mathrm{d}\Gamma_0 + \int_{\Omega_0} \rho_0 B_i^h(\mathbf{X}, t) N_I(\mathbf{X}) \mathbf{e}_i \, \mathrm{d}\Omega_0, \tag{15}$$

$$\mathbf{f}_I^{\mathrm{int}} = \int_{\Omega_0} P_{Ji}^h \frac{\partial N_I}{\partial X_J} \mathbf{e}_i \, \mathrm{d}\Omega_0, \tag{16}$$

where $\mathbf{e}_i,\ i = 1, 2, 3$ are the unit vectors of the referential coordinate system.

2.2. Energy equation

The rate form of balance of energy is

$$\int_{\Omega} \rho \dot{e} \, \mathrm{d}\Omega + \frac{\mathrm{d}}{\mathrm{d}t} \int_{\Omega} \frac{\rho}{2} \mathbf{v} \cdot \mathbf{v} \, \mathrm{d}\Omega = \int_{\partial\Omega} \mathbf{t} \cdot \mathbf{v} \, \mathrm{d}\Gamma - \int_{\partial\Omega} \mathbf{n} \cdot \mathbf{q} \, \mathrm{d}\Gamma, \tag{17}$$

where e is the specific internal energy, $\mathbf{v} = \mathrm{d}\mathbf{u}/\mathrm{d}t$, and $\mathbf{t}$ is the flux of mechanical force, or traction; and $\mathbf{q}$ is the heat flux vector through the boundary.

Considering the rate form of balance of mechanical energy, we have

$$\int_{\partial\Omega} \mathbf{t} \cdot \mathbf{v} \, \mathrm{d}\Gamma = \int_{\Omega} \boldsymbol{\sigma} : \mathbf{D} \, \mathrm{d}\Omega + \frac{\mathrm{d}}{\mathrm{d}t} \int_{\Omega} \frac{1}{\rho} \mathbf{v} \cdot \mathbf{v} \, \mathrm{d}\Omega. \tag{18}$$

Substituting Eq. (18) into Eq. (17) and pulling back Eq. (17) into the referential configuration yields

$$\int_{\Omega_0} \rho_0 \dot{e}\, \mathrm{d}\Omega_0 = \int_{\Omega_0} \boldsymbol{\tau} : \mathbf{D}\, \mathrm{d}\Omega_0 - \int_{\partial\Omega_0} J\hat{\mathbf{N}} \cdot \mathbf{F}^{-1} \cdot \mathbf{q}\, \mathrm{d}\Gamma_0, \tag{19}$$

in which, the standard volume/area transformations, $\mathrm{d}\Omega = J\,\mathrm{d}\Omega_0$, $J = \det\{\mathbf{F}\}$, $\hat{\mathbf{n}}\,\mathrm{d}\Gamma = J\hat{\mathbf{N}}\mathbf{F}^{-1}\,\mathrm{d}\Gamma_0$, are used, where $\hat{\mathbf{n}}$ and $\hat{\mathbf{N}}$ are the outward normals of surface elements in the spatial and the referential configurations, respectively.

We neglect thermo-elastic contribution on internal work, i.e. $\boldsymbol{\tau} : (\mathbf{D}^{\mathrm{e}} + \mathbf{D}^{\mathrm{t}}) \approx 0$, and assume that the main part of plastic work is converted into heat [44]. Using the specific heat at constant pressure, C_{p}, to approximate the specific heat at constant stress, one may be able to derive the energy equation featured with adiabatic viscous heating

$$\rho_0 C_{\mathrm{p}} \frac{\partial T}{\partial t} = \chi \boldsymbol{\tau} : \mathbf{D}^{\mathrm{vp}} + \nabla_{\mathbf{X}}\left(J\mathbf{F}^{-1} \cdot \boldsymbol{\kappa} \cdot \mathbf{F}^{-\mathrm{T}} \cdot \nabla_{\mathbf{X}} T\right) \quad \forall \mathbf{X} \in \Omega_0. \tag{20}$$

Because the entire impact process lasts only a few hundred μs, the effect of heat conduction may be negligible. Considering adiabatic heating, i.e. neglecting heat transfer, we have

$$\rho_0 C_{\mathrm{p}} \frac{\partial T}{\partial t} = \chi \boldsymbol{\tau} : \mathbf{D}^{\mathrm{vp}}. \tag{21}$$

By doing so, the coupled thermo-elasto-viscoplastic problem is reduced to a mechanical problem. So the momentum equation, Eq. (9), suffices for constructing Galerkin weak form, and the energy equation (21) is only used in the constitutive update.

2.3. Constitutive update

A rate form constitutive equation is used

$$\overset{\triangledown}{\boldsymbol{\tau}} := \mathbf{C}^{\mathrm{elas}}(\mathbf{D} - \mathbf{D}^{\mathrm{vp}} - \mathbf{D}^{\mathrm{t}}), \tag{22}$$

where the Jaumann rate of Kirchhoff stress, $\overset{\triangledown}{\boldsymbol{\tau}}$, is defined as

$$\overset{\triangledown}{\boldsymbol{\tau}} = \dot{\boldsymbol{\tau}} - \mathbf{W} \cdot \boldsymbol{\tau} + \boldsymbol{\tau} \cdot \mathbf{W}. \tag{23}$$

A thermo-elasto-viscoplastic material model is adopted (see [51]), which is described as

$$D_{ij}^{\mathrm{vp}} := \bar{\eta}(\bar{\sigma}, \bar{\epsilon}, T)\frac{\partial f}{\partial \sigma_{ij}}, \tag{24}$$

$$\bar{\eta} = \dot{\epsilon}_0 \left[\frac{\bar{\sigma}}{g(\bar{\epsilon}, T)}\right]^m, \tag{25}$$

$$g(\bar{\epsilon}, T) = \sigma_0\left[1 + \bar{\epsilon}/\epsilon_0\right]^N \left\{1 - \delta\left[\exp\left(\frac{T - T_0}{\kappa}\right) - 1\right]\right\}, \tag{26}$$

$$\bar{\epsilon} := \int_0^{\mathrm{t}} \sqrt{\frac{2}{3}\mathbf{D}^{\mathrm{vp}} : \mathbf{D}^{\mathrm{vp}}}\, \mathrm{d}t, \tag{27}$$

where m is the power index, $\dot{\epsilon}_0$ is the referential strain rate, σ_0 is the yield stress, $\epsilon_0 = \sigma_0/E$, and δ is the thermal softening parameter. The thermal rate of deformation, $\mathbf{D}^{\mathrm{t}}$, is given as

$$\mathbf{D}^{\mathrm{t}} = \alpha \dot{T}\mathbf{1}, \tag{28}$$

where α is the coefficient of thermal expansion, and $\mathbf{1}$ is the identity matrix.

Constitutive update follows the adiabatic rate tangent modulus formula explained in [25]. The essence of the rate tangent modulus method is to approximate a function of time in the interval $t_{n+\theta} \in [t_n, t_{n+1}]$, $\theta \in [0, 1]$, as

$$f_\theta := (1-\theta)f_n + \theta f_{n+1}. \tag{29}$$

For kinematic variables, this may fall into a special case of standard Newmark-β method. However, a non-trivial task is to update the Kirchhoff stress. The following approximation is used in constitutive update:

$$\boldsymbol{\tau}_{n+1} = \boldsymbol{\tau}_n + \dot{\boldsymbol{\tau}}_\theta \Delta t, \tag{30}$$

$$\dot{\boldsymbol{\tau}}_\theta \approx \overset{\triangledown}{\boldsymbol{\tau}}_\theta + \mathbf{W}_\theta \cdot \boldsymbol{\tau}_n + \boldsymbol{\tau}_n \cdot \mathbf{W}_\theta^{\mathrm{T}}, \tag{31}$$

where

$$\overset{\triangledown}{\boldsymbol{\tau}}_\theta = \mathbf{C}_\theta^{\tan} : \mathbf{D}_\theta - \left\{ \frac{\dot{\bar{\epsilon}}_n}{1+\xi_\theta} \right\} \left[\mathbf{P}_\theta + 3K\alpha \frac{\chi \bar{\sigma}_\theta}{\rho C_{\mathrm{p}}} \mathbf{1} \right], \tag{32}$$

where

$$\mathbf{C}_\theta^{\tan} = \mathbf{C}^{\mathrm{elas}} - \frac{\xi_\theta}{H_\theta(1+\xi_\theta)} \left[\mathbf{P}_\theta \otimes \mathbf{P}_\theta + (3\lambda + 2\mu)\alpha \frac{\chi \bar{\sigma}_n}{\rho_0 C_{\mathrm{p}}} \mathbf{1} \otimes \mathbf{P}_\theta \right], \tag{33}$$

is the adiabatic tangent stiffness, and it is not symmetric. Assuming that $\bar{\epsilon}_\theta$ and $\bar{\sigma}_\theta$ are available after the stress update, the temperature field is updated at each quadrature point

$$T_{n+1} = T_n + \dot{T}_\theta \Delta t, \tag{34}$$

where

$$\dot{T}_\theta = \frac{\chi}{\rho_0 C_{\mathrm{p}}} \dot{\bar{\epsilon}}_\theta \bar{\sigma}_\theta. \tag{35}$$

2.4. Modeling stress collapsing state of shear band

How and why a strain localization zone is able to propagate has not been well understood until today. This reflects a lack of theoretical understanding, as well as a lack of successful numerical simulations. In many simulations, the initial strain localization zone simply does not propagate. As shown by Gioia and Ortiz [12], the stress field near the initial strain localization zone at the pre-notch tip in a thermo-elastic-viscoplastic material is somewhat diffusive. This has been confirmed in the numerical analysis by Needleman [37] for an elasto-viscoplastic material. This "diffusive" nature of the stress field in front of the "tip" of strain localization zone seems to retard the advance of the material instability. In fact, until this date, the notion that a shear band, or a strain localization zone in a solid represented by a simple constitutive relation, can automatically advance under external load as a crack has never been verified in numerical computations.

On the other hand, based on Marchand and Duffy's experiments [32], there are three stages in the development of adiabatic shear band formation. In the third – the final stage, the effective strain is up to more than 40%, and flow stresses begin to drop rapidly. This stress collapsing phenomenon in the localization zone has been also predicted by the theoretical study by Wright and his co-workers [46,49]. The main assumption of this work is that the stress collapsing within the fully developed shear band will significantly reduce the shear stress carrying capability of the localization zone, and it will lead to the localized strain rate concentration at the shear band tip, and thus initiate the advancement of the localization zone. In other words, stress collapsing is the key for dynamic shear band propagation.

Based on this premise, the crucial technical ingredient for simulating dynamic shear band propagation is how to model the stress collapsing state of the adiabatic shear band. Zhou et al. [51] modeled the stress collapsing state as a "Newtonian fluid", and by doing so they appeared to be the first group of people to be able to simulate the dynamic shear band propagation. Li et al. [25] used a similar fluid model in a 3D meshfree simulation, and they accurately replicated dynamic shear band propagation, failure mode

transition, as well as curved shear band formations. In this study, we use a separate constitutive relation to model the stress collapsing state inside the adiabatic shear band, and view this type of approach as a multiple physics modeling. Since the stress collapsing region inside the shear band is of the order of μm, the use of multiple physics model is appealing.

It is well known that plastic deformation is caused by dislocation movement. On the other hand, adiabatic shear band in crystalline is characterized by local high temperature rise (up to metal's melting point) , and high strain rate (up to 10^4–10^6 s^{-1}). At high temperature and high strain rate, lattice vibration becomes the major obstacle for dislocation motion, which is often referred to as phonon drag. The physical process is rate sensitive, and temperature-dependent. Two types of phenomenological constitutive laws have been used in the literature to describe the inelastic deformation under high temperature and strain rate loading conditions. The first type is a temperature-dependent deformation mechanism that is modeled by an Arrhenius-type law [7,45] as follows:

$$\tau = \tau_0 \exp\left\{-\beta\left[\frac{\theta}{\theta_0} - 1\right]\right\}\left(\frac{\dot{\gamma}}{\dot{\gamma}_0}\right)^m, \tag{36}$$

where τ_0, $\dot{\gamma}_0$, and θ_0 are the reference stress, strain rate, and temperature. A 3D generalization of (36)

$$\sigma_{ij} = -p\delta_{ij} + 2\exp\left[-\beta(\theta - 1)\right]\dot{\gamma}^{m-1}D_{ij} \tag{37}$$

has been used by Molinari and Leroy [19,34,35]) to model the shear band that occurs in the ductile shear zones of the earth's lower crust. Eq. (37) is in fact a constitutive relation for a non-Newtonian fluid.

Another type of constitutive law used under high strain rate condition is based on the experimental data of Campbell and Ferguson [5]

$$\dot{\gamma}^p = \dot{\gamma}_t + \dot{\gamma}_0\frac{(\tau - \tau_t)}{\mu} \quad \forall \dot{\gamma}^p \geqslant \dot{\gamma}_t, \tag{38}$$

where μ is the elastic shear modulus at the temperature in question, and τ_t is the transition shear stress associated with $\dot{\gamma}_t$. And $\dot{\gamma}_t$, $\dot{\gamma}_0$ are constants depending on material's properties at high strain rate. Eq. (38) is basically a statement that under high strain rate and high temperature condition the shear stress increment is proportional to the increment of shear strain rate, since when $\dot{\gamma}_p \geqslant \dot{\gamma}_t$, the deformation state is up to the phonon drag control region. Similar constitutive equations of plastic flow at high strain rate were compiled by Frost and Ashby [11]. The simple relation (38) is generalized into a 3D formulation by Freund and Hutchinson [10] in their study of crack growth under high strain rate condition, which is now known as the Freund–Hutchinson theory

$$D_{ij}^{\mathrm{p}} = \frac{1}{2}\frac{F(\tau)}{\tau}s_{ij}, \quad \text{where } F(\tau) = \dot{\gamma}_t + \dot{\gamma}_0(\tau - \tau_t)/\mu, \tag{39}$$

where s_{ij} is the deviatoric stress tensor. And

$$D_{ij}^{\mathrm{e}} = \frac{1+v}{E}\dot{\sigma}_{ij} - \frac{v}{E}\dot{\sigma}_{kk}\delta_{ij}. \tag{40}$$

If one neglects deviatoric elastic deformation, which is small in the high strain rate region, and the constant term $\dot{\gamma}_t - \dot{\gamma}_0\tau_t/\mu$, the plastic deformation described in Eq. (39) resembles a Newtonian fluid motion. Note that one may rewrite $F(\tau)$ as

$$F(\tau) = \frac{\dot{\gamma}_0}{\mu}(\tau + \mu\dot{\gamma}_t/\dot{\gamma}_0 - \tau_t). \tag{41}$$

The constant term $\mu\dot{\gamma}_t/\dot{\gamma}_0 - \tau_t$ might be interpreted as stress drop, and it may be set to 0 in the stress collapsing zone.

Combining the above two approaches, we use the following constitutive equations to model the stress collapsing state in the core region of the adiabatic shear band:

$$\sigma_{ij} = -p\delta_{ij} + \mu^*(T)D_{ij}, \tag{42}$$

where the shear modulus or viscosity coefficient can be temperature dependent, such as

$$\mu^*(T) = \mu_0 \exp\left[-\beta\left(\frac{T - T_0}{T_0}\right)\right], \tag{43}$$

where β is an empirical constant. The equation of state is the usual thermo-elastic relation

$$p = K^*(-e + \alpha(T - T_0)), \tag{44}$$

where $e = \partial u_i/\partial x_i$, i.e. volumetric expansion, K^* is the elastic bulk modulus, and α is the linear coefficient of thermal expansion. In the context of large deformation, Eq. (42) is replaced by

$$\tau_{ij} = -K^*[1 - J + \alpha(T - T_0)]\delta_{ij} + \mu^*(T)D_{ij}, \tag{45}$$

where τ_{ij} is the component of Kirchhoff stress tensor; $J := \det|\mathbf{F}|$. Since the rate of deformation tensor is always objective in any coordinate system, once the rate of deformation is obtained, one can immediately update the Kirchhoff stress. Generalizing the Talyor and Quinney law [44], one may assume that

$$\rho_0 C_{\mathrm{p}} \frac{DT}{Dt} = \chi\tau : \mathbf{D}, \quad 0 < \chi \leqslant 1. \tag{46}$$

The constitutive update of stress collapsing region is as follows:

$$\boxed{\begin{array}{l} \textit{Step } 1. \quad \tau_{ij}^{n+1} = -K^*\left[1 - J^{n+1} + \alpha(T_n - T_0)\right]\delta_{ij} + \mu^*(T_n)D_{ij}^{n+1} \\ \textit{Step } 2. \quad T_{n+1} = T_n + \dfrac{\chi}{\rho_0 C_{\mathrm{p}}}\tau_{ij}^{n+1}D_{ij}^{n+1}\Delta t \end{array}} \tag{47}$$

In our preliminary study, we neglected the temperature dependence on μ (in our formulation, the spatial density $\rho(T)$ is a function of temperature rise, which may not look apparent in a Lagrangian formula). The threshold at which a material point enters stress collapsing phase is controlled by the following empirical criterion proposed by Zhou et al. [51]:

$$\bar{\epsilon}_{\mathrm{cr}} = \epsilon_1 + (\epsilon_2 - \epsilon_1)\frac{\dot{\epsilon}_r}{(\dot{\epsilon}_r + \dot{\bar{\epsilon}})}, \tag{48}$$

where ϵ_1, ϵ_2 and $\dot{\epsilon}_r$ are empirical the parameters depending on material's properties. When the effective strain of a material points reaches to $\bar{\epsilon}_{\mathrm{cr}}$, the material point is considered in the stress collapsing state, and Eq. 47 is used in state variable update.

3. Numerical simulation of asymmetric impact problem

3.1. Overview

The computations carried out in this work focus on simulating the experiments conducted by Zhou et al. [52], i.e. the ZRR problem. The experiment involves an asymmetrically impact loading of a pre-notched plate (single notch) by a cylindrical projectile as shown in Fig. 2. In this numerical study, two configurations have been used to simulate plate specimens of different sizes, which correspond to two different sets of experiments. The first configuration models the experiment conducted by Zhou et al. [52] (see Fig. 3(a)), while the second one models the experiments conducted recently by Guduru et al. [14] (see Fig. 3(b)). It may be noted that in the second specimen, there is a 2 mm long fatigue crack in front of the pre-notch, which increases the acuity of the crack. We have conducted both 2D and 3D simulations for the first specimen: a 3D computation with projectile speed at $V = 30$ m/s, and 3D computation with projectile speed at

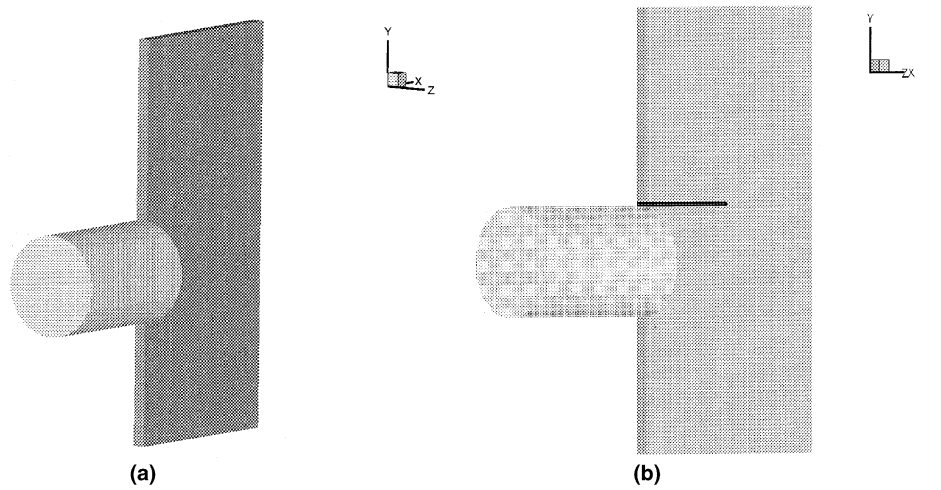

Fig. 2. An asymmetrically impact-loaded plate with a pre-notched crack.

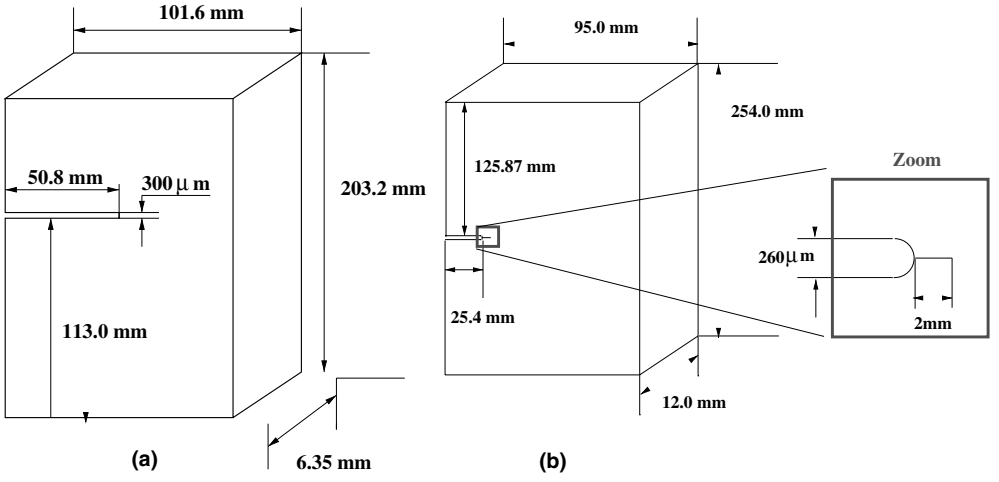

Fig. 3. Configuration of single notch specimens: (a) specimen one; (b) specimen two.

$V = 33$ m/s. For the second specimen, we have only carried out a 2D computation with projectile speed at $V = 37$ m/s.

The primary objectives of these simulations are twofold: (1) to capture failure mode transition; (2) to determine the adiabatic shear band growth criterion and driving force.

3.2. Case I: Intermediate speed impact ($V = 30$ m/s)

In the experiment conducted by Zhou et al. [52], when the impact velocity is in the intermediate range, i.e. 20.0 m/s $< V <$ 30.0 m/s, a shear band initiates from the notch tip, and it is then arrested within the specimen interior. The final failure of the specimen is caused by brittle fracture – a cleavage-type (mode-I) crack growing from the end of the arrested shear band. This shearband-crack switch under fixed impact speed is intriguing, whose causes are not understood well. It is therefore of considerable challenge to simulate such a failure mode switching phenomenon. The main parameters in our simulations are listed in Table 1.

Table 1
Material properties of the target plate

Parameter	Value	Definition
$\dot{\epsilon}_0$	1×10^{-3} s^{-1}	Reference strain rate
m	70	Rate sensitivity parameter
σ_0	2000 MPa	Yield stress
ϵ_0	σ_0/E	
n	0.01	Strain hardening exponent
T_0	293 K	Reference temperature
δ	0.8	Thermal softening parameter
κ	500 K	Thermal softening parameter
E	200 GPa	Young's modulus
ν	0.3	Poisson's ratio
ρ	7830 kg/m^3	Mass density
c_p	448 J/(kg K)	Specific heat
α	11.2×10^{-6} K^{-1}	Coefficient of thermal expansion
χ	0.9	The fraction of plastic work converted to heat
ϵ_1	$4.0 \times \epsilon_0$	
ϵ_2	0.3	
$\dot{\epsilon}_r$	4.0×10^4 s^{-1}	In a range (1.0×10^4–6.0×10^4 s^{-1})

Fig. 4(a)–(f) shows a sequence of effective stress contours (SS [Pa]) surrounding the failure region following the impact. It can be clearly observed that a strip – a low effective stress zone initiates, and grows starting from the notch tip, which we identify as the trace of adiabatic shear band. The shear band grows steadily almost in the horizontal direction. At a certain point (Fig. 4(c)), it suddenly changes its direction and moves upward. At this time within the strip, the value of effective stress vanishes, which indicates that a crack is initiated from the tip of the shear band. We identify this turning point as the point at which the shear band transits into an opening crack (see Fig. 4(d)–(f)). To view the shearband-to-crack switch clearly, a 3D view of the plate under impact of the projectile is displayed in Fig. 5(a), (b). The color contour depicted on the surface of the specimen is effective stress (SS [Pa]), from which one may compare the initial stage of shear band growth with the final stage of crack growth. In Fig. 5(a) (24.0 μs after impact), there is only a shear band in front of pre-notch. As the process continues, from Fig. 5(b), one can observe that a crack is running away from the arrested shear band. In our previous study [25], the impact is simulated as a prescribed velocity condition at the impact zone. The prescribed impact velocity is a linear ramp between 0 and 0.5 μs, it reaches 30 m/s at $t = 0.5$ μs and keeps constant until $t = 47$ μs (Fig. 6).

In the current simulation, the impact between the projectile and the plate is modeled as a real collision between a rigid cylinder projectile and a visco-elasto-plastic solid plate. One can compare the impact velocity histories of projectiles of two different approaches (see Figs. 6 and 7).

In the computation, a total of 49,086 particles are used to discretize the plate, and 32,080 background cells are allocated for the numerical quadrature. There are eight quadrature points in each background cell, for a total of 256,640 Gauss quadrature points. For the projectile, a total 1299 particles and 792 background cells have been used in discretization. The density of the projectile is 7900 kg/m^3. The projectile is 125 mm long, and 50 mm in diameter.

3.3. Case II: High speed impact ($V = 33$ m/s)

When the impact velocity exceeds a certain limit, V_{SB}, [1] the cleavage fracture of mode-I crack is suppressed, the shear band initiated from the pre-notch tip never stops, and it propagates through the specimen. Since the impact is due to an unsymmetric collision between the projectile and plate, the shear band

[1] In the experiments conducted by Zhou et al. [51], this critical velocity is $V_{SB} = 29.6$ m/s for C-300 steel. This value is expected to be sensitive to material properties as well as pre-notch geometry and the size of the specimen used.

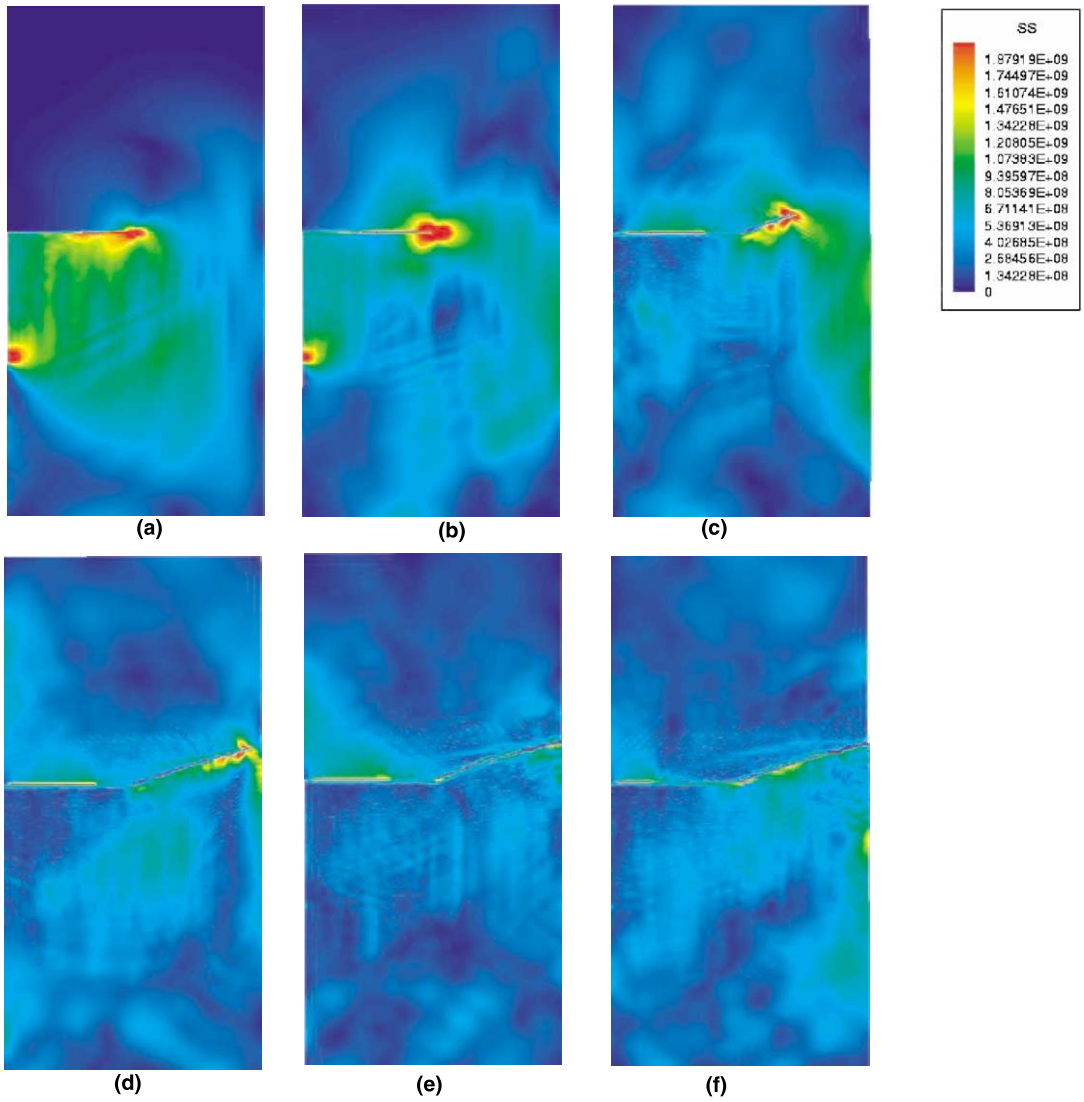

Fig. 4. Brittle-to-ductile failure mode transition (I) (brittle failure mode at $V = 30.0$ m/s): effective stress contour (SS [Pa]) of a 3D simulation (front plane view): (a) $t = 24$ μs; (b) $t = 36.0$ μs; (c) $t = 48.0$ μs; (d) $t = 60.0$ μs; (e) $t = 68.0$ μs; (f) $t = 76.0$ μs.

propagates slightly towards the lower part of the specimen, rather than propagating straight in the horizontal direction. A sequence of 3D calculations are displayed in Fig. 8. The color contours represent the effective stress (SS [Pa]) value. By examining the effective stress contours, one may notice that a thin strip with lower effective stress value passes through the specimen, which is the trace of the adiabatic shear band.

A sequence of 3D calculations have been displayed in Fig. 8, in which the effective stress contours are depicted, one may observe the evolution of the shear band from effective stress contours. By comparing the above results with the intermediate impact speed range, a complete picture of failure mode transition emerges, i.e. a transition from the cleavage fracture of a brittle failure at lower impact speeds to the shear propagation of a ductile failure at higher impact speeds.

As reported by Zhou et al. [51], the experimental results indicate that the shear band propagates along a curved surface. Such shear band morphology is very difficult to capture by finite elements, because of the generic mesh-alignment sensitivity in such simulations. Using meshfree methods, the curved shear band formation has been accurately captured in the numerical computations presented here.

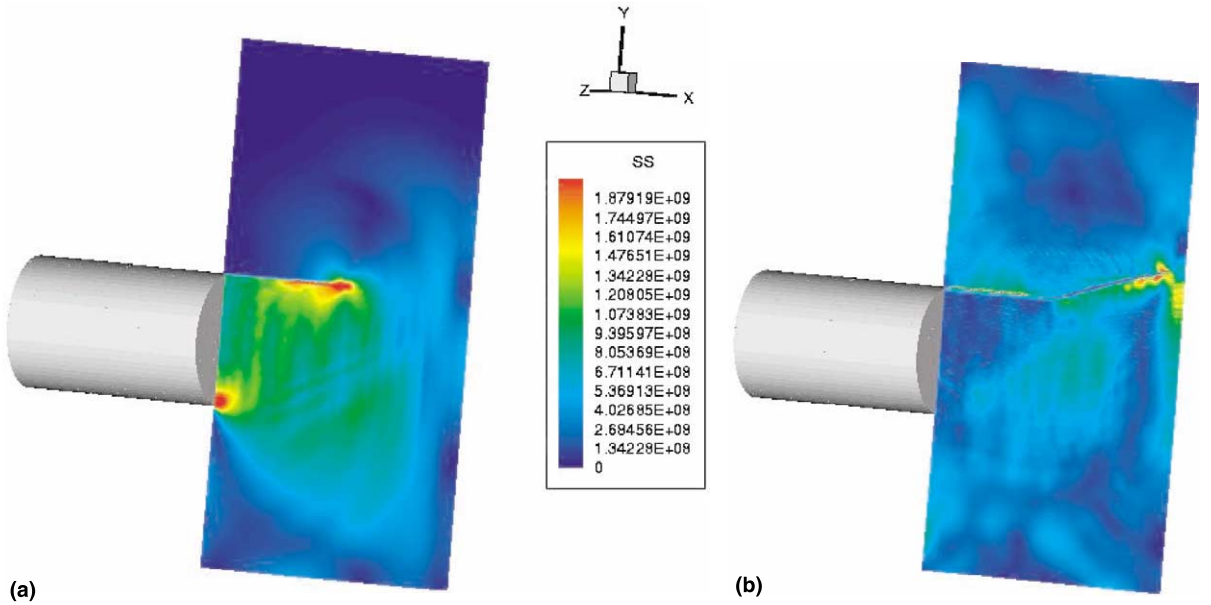

Fig. 5. Ductile-to-brittle failure mode switch: effective stress (SS [Pa]) of 3D simulation (3D view) with impact velocity $v = 30.0$ m/s: (a) $t = 24.0$ μs; (b) $t = 60.0$ μs.

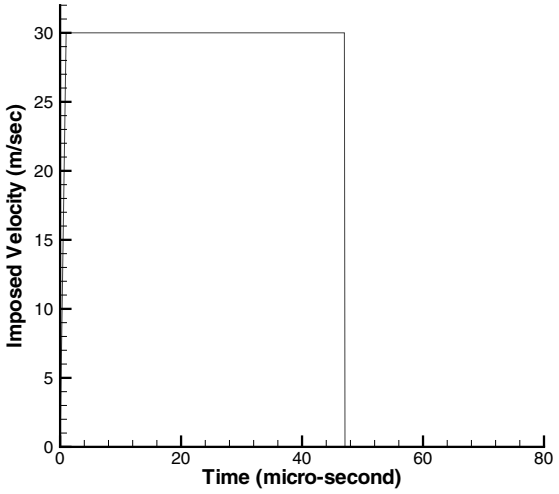

Fig. 6. The prescribed impact loading history in [25].

4. Micro-structure of shear band

4.1. Micro-structure of adiabatic shear band

In most of the previous studies of adiabatic shear band, the field variables, such as temperature, shear strain, or effective stress distributions are assumed to be uniform, and they are symmetrically distributed across the width of the shear band [8,40,41,47,48], which Wright [48] referred to as the so-called "canonical distributions". If one views the shear band model as a plastic flow confined between two rigid plates moving in opposition directions (compare the plane Couette flow), the conventional assumption is that this plastic flow is "essentially laminar" [14]. Recently, Guduru et al. [13,14] have used high speed optical and infrared

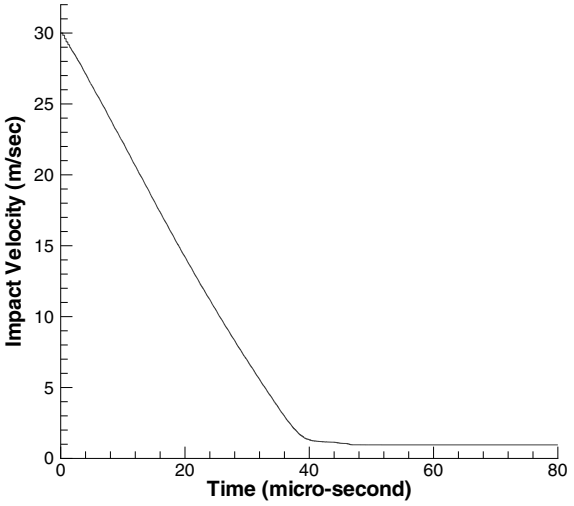

Fig. 7. The impact speed history of a rigid projectile colliding with the target.

techniques, such as 2D high speed infrared (IR) camera, to measure the temperature distribution within the dynamically propagating shear band. The IR images, for the first time, revealed that the temperature signature inside the adiabatic shear band is non-uniform, and it has short range spatial as well as temporal periodicity. This periodic high temperature distribution pattern, i.e. "hot spots", are in the middle of the shear band, which have a length scale from 100 to 300 μm.

The experimental observations [13] indicate that thermo-mechanical state inside the narrow adiabatic shear band is very active, and undergoes large fluctuations. This is in contrast with the conventional notion of micro-structure of shear band. The majority of the simple constitutive models paint a false picture of "platonic tranquility" inside the shear band.

Employing a multi-physics model described in Section 2 to model stress collapsing state inside the adiabatic shear band, we have simulated the exact experiment conducted by Guduru et al. [13,14] via meshfree Galerkin method with the exact same geometry and size of the specimen (Fig. 3(b)). A total of 79,742 particles are used in the meshfree discretization. In this testing specimen, there is a 2 mm fatigue crack in front of the pre-notch, which is modeled by using a meshfree visibility technique [3] to realize the discontinuity as shown in Fig. 9.

The numerical simulation confirms the experimental observation that there exists periodic "hot spots" in temperature distribution within the adiabatic shear band, and these periodic "hot spots" move down stream along the growing shear band. Since the width of the adiabatic shear band is very small, (100–300 μm), the temperature distribution inside the shear band can be hardly seen by the naked eyes. We zoom into the small box, a 1 mm × 1 mm area in front of the fatigue crack, to observe the transient micro-structure of adiabatic shear band. The zoom-in process is displayed in Fig. 10, which is a three-level magnification of temperature profile around the shear band region.

For the case of impact speed at 37 m/s, we compare the optical device measurement with numerical computation. The experimental results (Fig. 11(a)–(c)) are juxtaposed with numerical results (Fig. 11(d)–(f)). As shown in Fig. 11, there is a strong qualitative agreement between experimental data and numerical results. Also one may find that as time goes by, the experimental data show that the localized high temperature distribution starts to diffuse, or to spread out away from the shear band (yellow or green background in Fig. 11(a)–(c); whereas in numerical simulation, an adiabatic shear band model is adopted, therefore, the background of the temperature profile is always in blue color, because of the absence of heat transfer (cf. Fig. 12).

In addition, it has been found in the numerical simulation that such oscillatory temperature structure may have high-dimensional character (see Fig. 13). Furthermore, the oscillatory structure not only exists in temperature distribution, which is the only state variable susceptible to experimental measurement, but also exists in effective stress profile and effective strain profile as well (Fig. 13(a) and (b)). This suggests that we

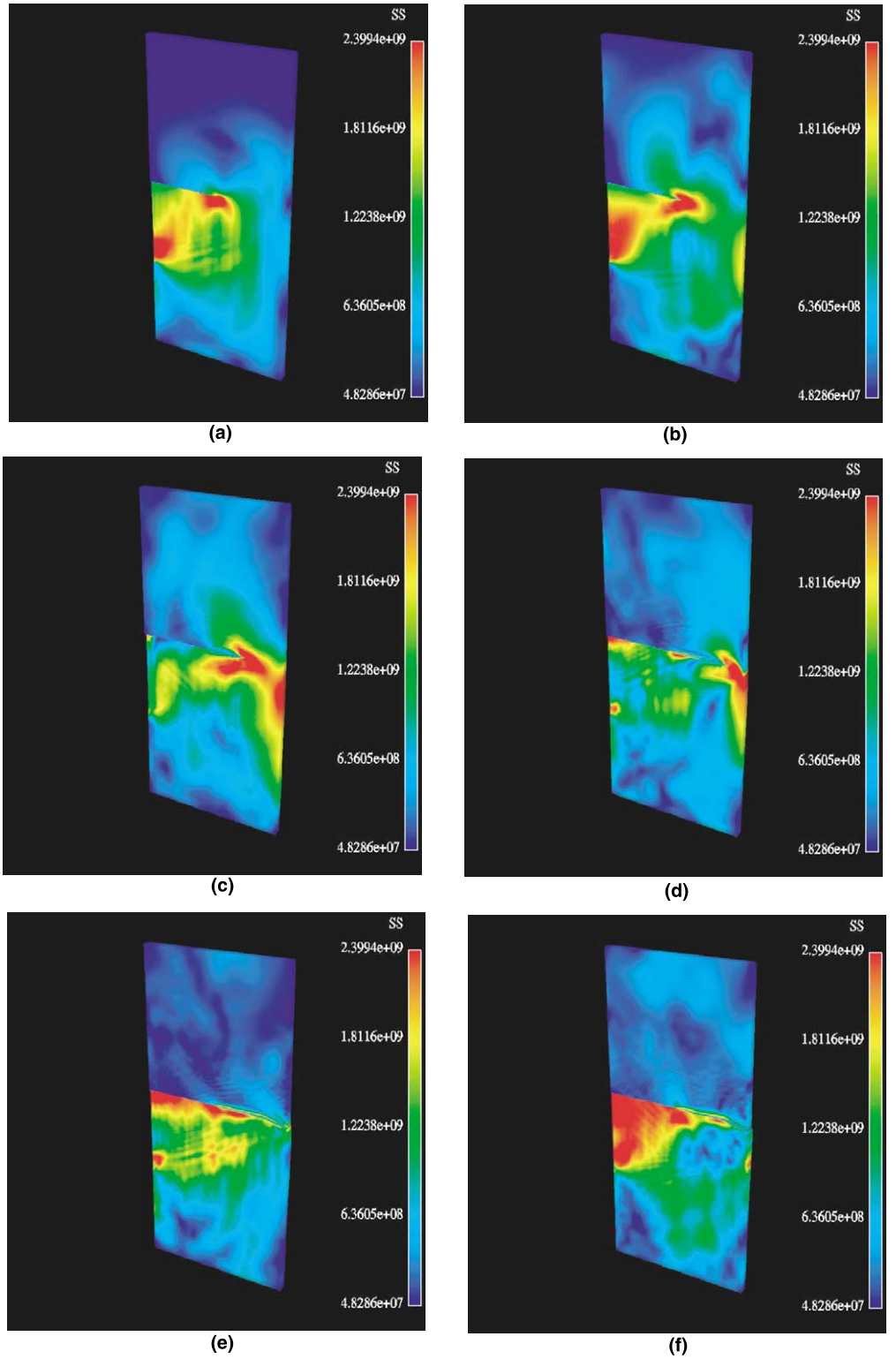

Fig. 8. Brittle-to-ductile transition (II) (ductile failure mode at $V = 33.0$ m/s): effective stress (SS [Pa]) contours of a 3D simulation. Values next to the scale bars are (top to bottom): 2.3994e + 09, 1.8116e + 09, 1.2238e + 09, 6.3605e + 08, 4.8286e + 07. (a) 24; (b) 36; (c) 48; (d) 60; (e) 68; (f) 76 μs.

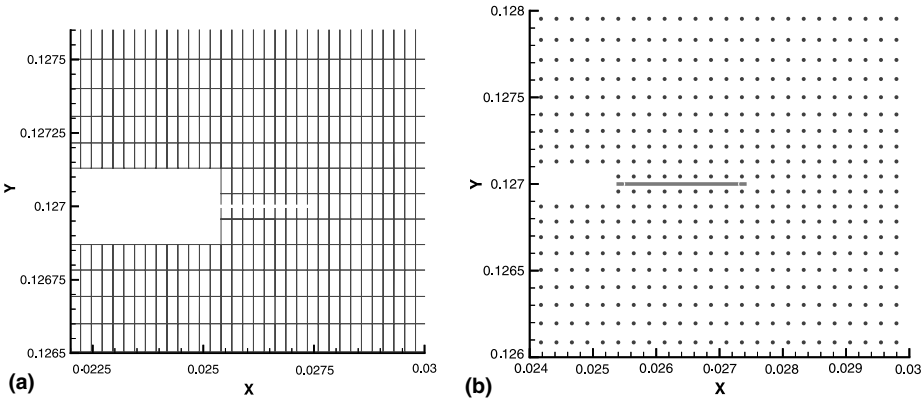

Fig. 9. Numerical modeling of a fatigue crack: (a) the fatigue crack configuration with mesh; (b) the fatigue crack (line) configuration without mesh.

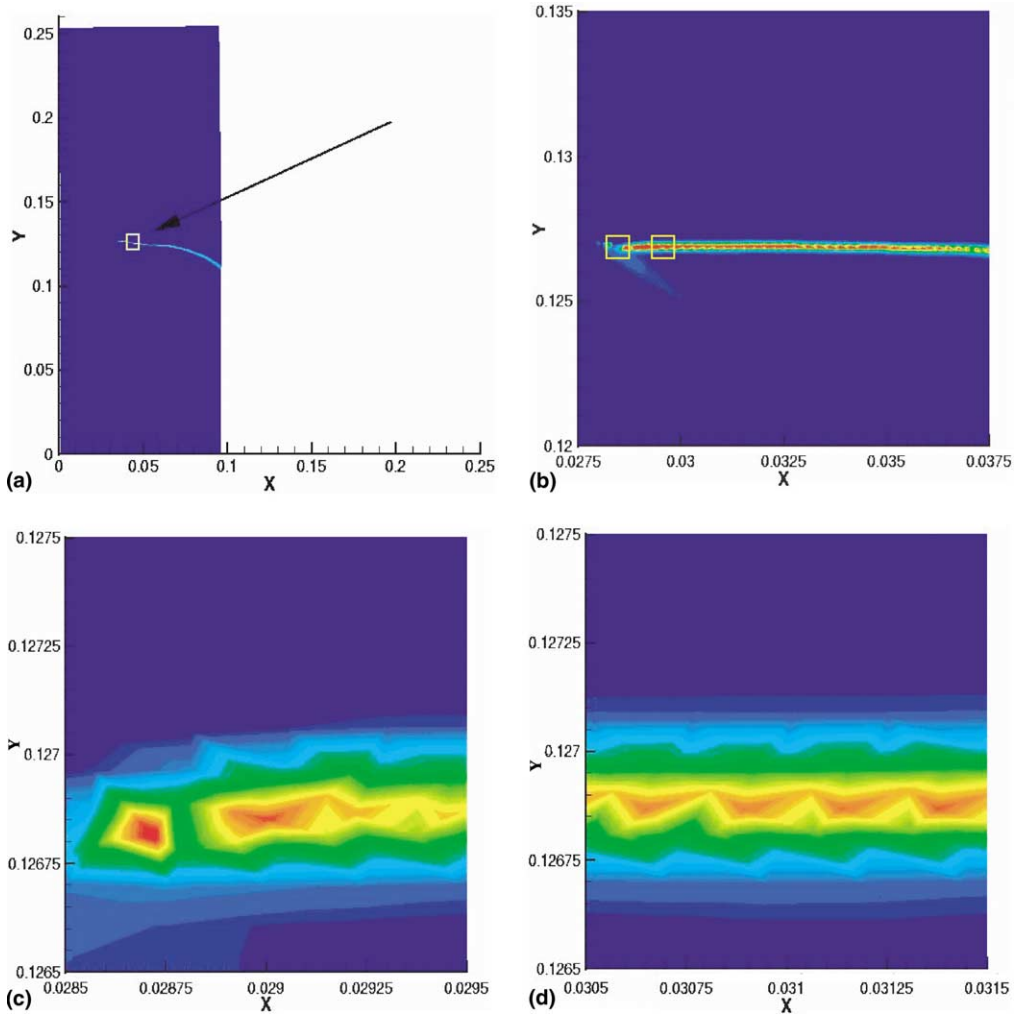

Fig. 10. The micro-structure (temperature profile) of adiabatic shear band: (a) level one; (b) level two; (c) level three (1); (d) level three (2).

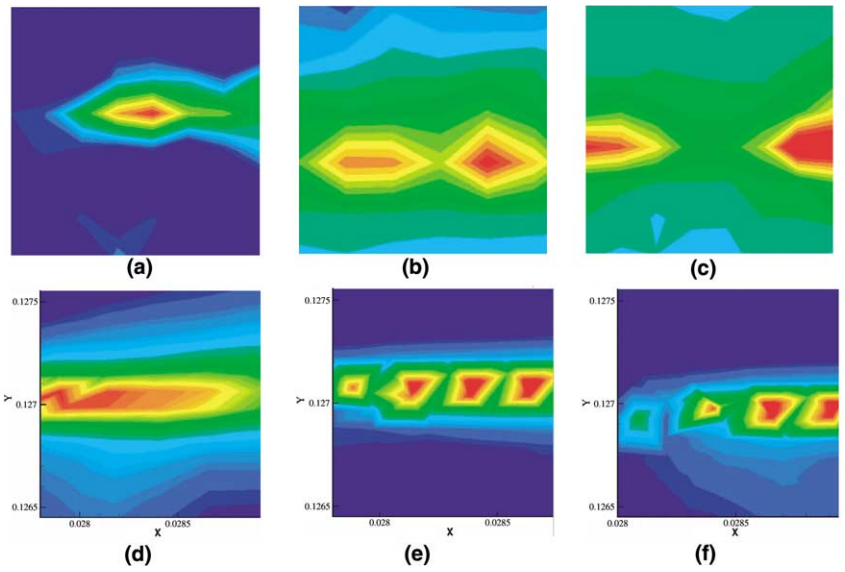

Fig. 11. Qualitative comparisons between experimental data and numerical computation on temperature distribution within the shear band ($V = 37$ m/s): (a), (d) $t = 12$ μs; (b), (e) $t = 36$ μs; (c), (f) $t = 72$ μs (experimental results: (a, b, c); numerical results: (d, e, f)).

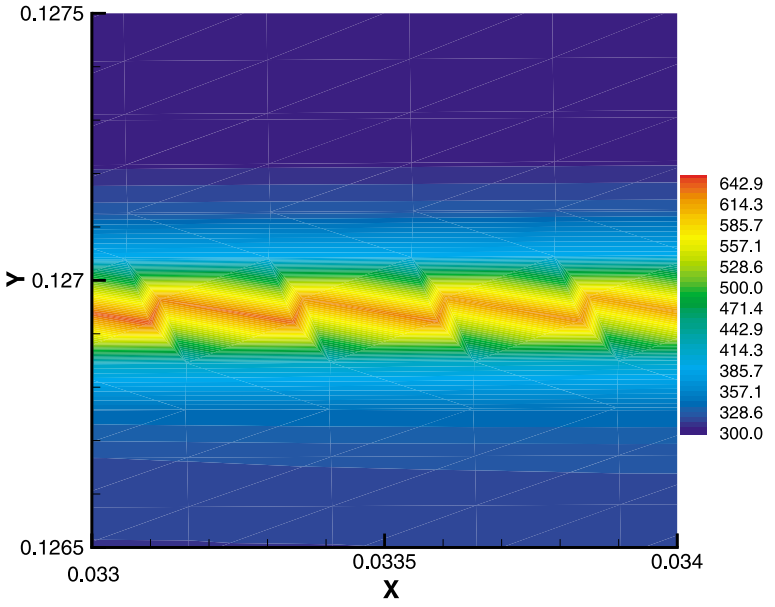

Fig. 12. The two-dimensional oscillation pattern in temperature profile (K).

may be observing a new type of thermal–mechanical instability within the adiabatic shear band, analogous to the classical instabilities in hydrodynamics (cf. Fig. 14).

For simplicity, one may simplify the adiabatic shear band problem as a 2D plane Couette problem with viscous heating (constant viscosity, or variable viscosity) due to the Taylor–Quinney mechanism. More precisely, we assume that the stress-collapsing zone can be approximated as a 2D plane Couette flow with viscous heating. Consider the Eulerian formulation of a multi-physics model of adiabatic shear band. Assume that the plastic shear flow is solenoidal. The governing equations of well-developed shear band zone (collapsing core) are as follows:

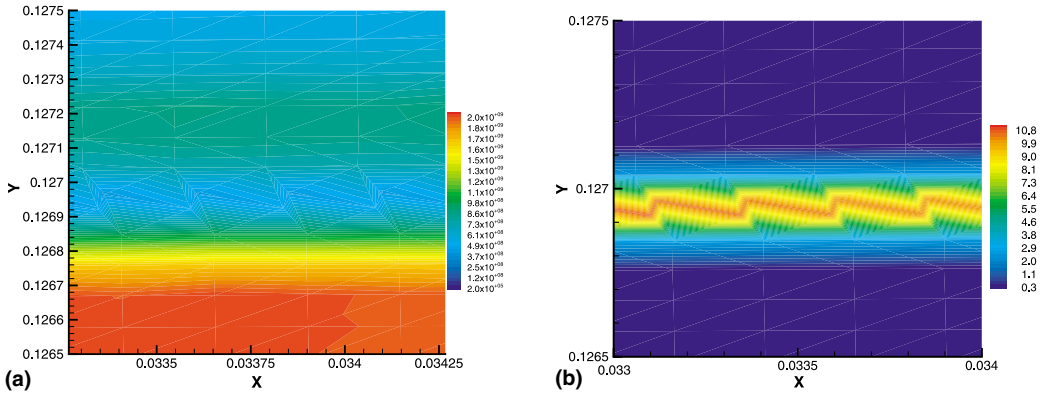

Fig. 13. The micro-structure of adiabatic shear band: (a) effective stress contour [Pa]; (b) effective strain contour (100%).

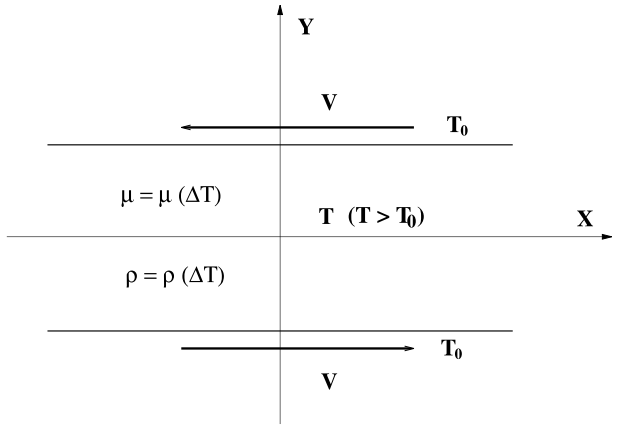

Fig. 14. Schematic illustration: plane Couette problem with viscous heating.

$$\frac{\partial v_i}{\partial t} + v_j \frac{\partial v_i}{\partial x_j} = \frac{\alpha K^*}{\rho(T)} \frac{\partial (T - T_0)}{\partial x_i} + \frac{\mu^*(T)}{\rho(T)} \nabla^2 v_i, \tag{49}$$

$$v_{i,i} = 0, \tag{50}$$

$$\frac{\partial T}{\partial t} + v_j \frac{\partial T}{\partial x_j} = \frac{\chi}{2\rho(T) C_{\mathrm{p}}} \sigma_{ij} \left(\frac{\partial v_i}{\partial x_j} + \frac{\partial v_j}{\partial x_i} \right), \tag{51}$$

where $\rho = \rho_0(1 - \alpha(T - T_0))$.

Some special cases, in which the viscosity–temperature relations derived from the Arrhenius-type law, or Nahme-type law, have been studied before [43,50]. It has been well established that if viscosity is temperature-dependent, hydrodynamic instability may occur. A temperature-dependent viscosity model has been used by Molinari and Leroy [19,34,35] to study the shear band formation in the earth's lower crust. A thermo-mechanical instability has been found in their analysis. As a matter of fact, in [35] the "hot spot" bifurcation solution is shown in numerical calculation. However, it is possible that in our multi-physics model with constant (kinematic) viscosity coefficient, a thermo-mechanical instability may still exist. The cause of the instability in this case could be due to the variance of temperature-dependent density. Under this situation, Boussinesq approximation (see [6,9]) may no longer be valid, because the temperature rise is of the order of 100–1000 K. Note that in the above formulation, the buoyancy force, the usual cause of thermo-mechanical instability in fluid, is not considered. A detailed linear perturbation analysis of system (49)–(51) will be presented elsewhere.

It is plausible that the dynamic micro-structure of adiabatic shear band shown here may have some influence on the ductile failure mechanism, or the brittle-to-ductile transition. The exact role of this possible instability on failure mode transition is not clear at the moment.

5. Concluding remarks

In this study, a meshfree method – reproducing kernel particle method is used in a displacement-based explicit formulation to simulate dynamic shear band propagation as well as micro-structures of adiabatic shear bands.

We have accomplished two things: first a complete failure mode transition (from impact speed $V = 30$ m/s to $V = 33$ m/s) has been replicated in meshfree simulation. When impact speed is below 30 m/s, under the mode-II loading, an adiabatic shear band is generated first, then quickly it turns into a cleavage mode-I crack. When projectile impact speed is above 30 m/s, say at 33 m/s, a shear band propagates through the pre-notched plate, showing ductile failure mechanism under higher strain rate condition. Second, numerical simulations have confirmed the early experimental observation that there exists a thermo-mechanical instability inside shear band, which might play a significant role in failure mode transition.

We conclude that the main advantages of using meshfree interpolants in simulations of dynamic shear band propagation are two: first, it can effectively avoid mesh-alignment sensitivity that finite element methods suffer; second it can relieve mesh distortion when modeling stress collapsing state of the adiabatic shear band as a purely plastic fluid in a Lagrangian formulation. In addition, this work has examined the validity of multi-physics model used in constitutive modeling of the stress collapsing state in the adiabatic shear band. By using multi-physics model, it first allows us to simulate dynamic shear band propagation; furthermore, it predicts a possible thermo-mechanical instability occurring inside the adiabatic shear band, which is either due to the viscous heating with thermo-mechanical coupling, or due to the viscous heating with temperature-dependent viscosity.

Acknowledgements

This work is supported by grants from the Army Research Office, National Science Foundation, and Tull Family Endowment.

References

[1] R.C. Batra, R.R. Gummalla, Effect of material and geometric parameters on deformations near the notch-tip of a dynamically loaded pre-noteched plate, Int. J. Fract. 101 (2000) 99–140.
[2] R.C. Batra, N.V. Nechitailo, Analysis of failure modes in impulsively loaded pre-notched steel plates, Int. J. Plast. 13 (1997) 291–308.
[3] T. Belytschko, Y. Krongauz, D. Organ, M. Fleming, P. Krysl, Meshless methods: an overview and recent developments, Comput. Methods Appl. Mech. Engrg. 139 (1996) 3–48.
[4] T. Belytschko, Y.Y. Lu, L. Gu, Element free Galerkin methods, Int. J. Numer. Methods Engrg. 37 (1994) 229–256.
[5] J.D. Campbell, W.G. Ferguson, The temperature and strain-rate dependence of the shear strength of mild steel, Philos. Mag. 21 (1970) 63–82.
[6] S. Chandrasekhar, Hydrodynamic and Hydromagnetic Stability, Oxford University Press, Oxford, 1961.
[7] R.J. Clifton, Dynamic plasticity, ASME J. Appl. Mech. 50 (1983) 941–952.
[8] F. Dinzart, A. Molinari, Structure of adiabatic shear bands in thermo-viscoplastic materials, Eur. J. Mech. A 17 (1998) 923–938.
[9] P.G. Drazin, W.H. Reid, Hydrodynamic Stability, Cambridge University Press, Cambridge, 1981.
[10] L.B. Freund, J.W. Hutchinson, High strain-rate crack growth in rate-dependent plastic solids, J. Mech. Phys. Solids 33 (1985) 169–191.
[11] H.J. Frost, M.F. Ashby, Deformation-Mechanism Maps, Pergamon Press, Oxford, 1982.
[12] G. Gioia, M. Ortiz, The two-dimensional structure of dynamic boundary layers and shear bands in thermoviscoplastic solids, J. Mech. Phys. Solids 44 (1996) 251–291.
[13] P. Guduru, G. Ravichandran, A.J. Rosakis, Observations of transient high temperature vortical microstructure in solids during adiabatic shear banding, Mech. Mater., submitted.

[14] P. Guduru, A.J. Rosakis, G. Ravichandran, Dynamic shear bands: an investigation using high speed optical and infrared diagnostics, Mech. Mater., submitted.
[15] J.F. Kalthoff, Shadow optical analysis of dynamic shear fracture, SPIE Photomech. Speckle Metrol. 814 (1987) 531–538.
[16] J.F. Kalthoff, Transition in the failure behavior of dynamically shear loaded crack, Appl. Mech. Rev. 43 (1990) S247–S250.
[17] J.F. Kalthoff, Modes of dynamic shear failure in solids, Int. J. Fract. 101 (2000) 1–31.
[18] J.F. Kalthoff, S. Winkler, Failure mode transition at high rates of shear loading, in: C.Y. Chiem, H.-D. Kunze, L.W. Meyer (Eds.), Impact Loading and Dynamic Behavior of Materials, 1987, pp. 185–195.
[19] Y.M. Leroy, A. Molinari, Stability of steady states in shear zones, J. Mech. Phys. Solids 40 (1992) 181–212.
[20] S. Li, W. Hao, W.K. Liu, Numerical simulations of large deformation of thin shell structures using meshfree methods, Comput. Mech. 25 (2/3) (2000) 102–116.
[21] S. Li, W. Hao, W.K. Liu, Meshfree simulation shear banding under large deformation, Int. J. Solids Struct. 37 (2000) 7185–7206.
[22] S. Li, W.K. Liu, Reproducing kernel hierarchical partition of unity part i: formulation & theory, Int. J. Numer. Methods Engrg. 45 (1999) 251–288.
[23] S. Li, W.K. Liu, Reproducing kernel hierarchical partition of unity part ii: applications, Int. J. Numer. Methods Engrg. 45 (1999) 288–317.
[24] S. Li, W.K. Liu, Numerical simulations of strain localization in inelastic solids using meshfree methods, Int. J. Numer. Methods Engrg. 48 (2000) 1285–1309.
[25] S. Li, W.K. Liu, A.J. Rosakis, T. Belytschko, W. Hao, Meshfree Galerkin simulations of dynamic shear band propagation, Int. J. Solids Struct., submitted.
[26] W.K. Liu, Y. Chen, S. Jun, J.S. Chen, T. Belytschko, C. Pan, R.A. Uras, C.T. Chang, Overview and applications of the reproducing kernel methods, Arch. Comput. Methods Engrg. 3 (1996) 3–80.
[27] W.K. Liu, Y. Chen, R.A. Uras, C.T. Chang, Generalized multiple scale reproducing kernel particle methods, Comput. Methods Appl. Mech. Engrg. 139 (1996) 91–158.
[28] W.K. Liu, S. Jun, S. Li, J. Adee, T. Belytschko, Reproducing kernel particle methods for structural dynamics, Int. J. Numer. Methods Engrg. 38 (1995) 1655–1679.
[29] W.K. Liu, S. Jun, Y. Zhang, Reproducing kernel particle methods, Int. J. Numer. Methods Fluids 20 (1995) 1081–1106.
[30] W.K. Liu, S. Li, T. Belytschko, Moving least square reproducing kernel method part i: methodology and convergence, Comput. Methods Appl. Mech. Engrg. 143 (1997) 422–433.
[31] W.K. Liu, R.A. Uras, Y. Chen, Enrichment of the finite element method with reproducing kernel particle method, ASME J. Appl. Mech. 64 (1997) 861–870.
[32] A. Marchand, J. Duffy, An experimental study of the formation process of adiabatic shear bands in a structural steel, J. Mech. Phys. Solids 38 (1988) 251–283.
[33] J.J. Mason, A.J. Rosakis, G. Ravichandran, Full field measurement of the dynamic deformation field around a growing adiabatic shear band at the tip of a dynamically loaded crack or notch, J. Mech. Phys. Solids 42 (1994) 1679–1697.
[34] A. Molinari, Y.M. Leroy, Existence and stability of stationary shear bands with mixed-boundary conditions, C.R. Acad. Sci. Paris, Ser. II 310 (1990) 1017–1023.
[35] A. Molinari, Y.M. Leroy, Structures in shear zones due to thermal effects, C.R. Acad. Sci. Paris, Ser. II 313 (1991) 7–13.
[36] B. Nayroles, G. Touzot, P. Villon, Generalizing the finite element method: diffuse approximation and diffuse elements, Comput. Mech. 10 (1992) 307–318.
[37] A. Needleman, Dynamic shear band development in plane strain, J. Appl. Mech. 56 (1989) 1–9.
[38] A. Needleman, V. Tvergaard, Analysis of a brittle–ductile transition under dynamic shear loading, Int. J. Solids Struct. 32 (1995) 2571–2590.
[39] A. Needleman, V. Tvergaard, Numerical modeling of the ductile–brittle transition, Int. J. Fract. 101 (2000) 73–97.
[40] J.A. Oilellio, W.E. Olmstead, Shear band formation due to a thermal flux inhomogeneity, SIAM J. Appl. Math. 57 (1997) 959–971.
[41] J.A. Oilellio, W.E. Olmstead, Temporal evolution of shear band thickness, J. Mech. Phys. Solids 45 (1997) 345–359.
[42] K. Ravi-Chandar, On the failure mode transitions in polycarbonate dynamic mixed-mode loading, Int. J. Solids Struct. 32 (1995) 925–938.
[43] P.C. Sukanek, C.A. Goldstein, R.L. Laurence, The stability of plane couette flow with viscous heating, J. Fluid Mech. 57 (1973) 651–670.
[44] G.I. Taylor, H. Quinney, The latent energy remaining in a metal: after cold working, Proc. R. Soc. A 143 (1934) 307–326.
[45] J. Weertman, J.R. Weertman, High temperature creep of rock and mantle viscosity, in: F.A. Donath (Ed.), Annual Review of Earth and Planetary Science, Annual Review Inc., Palo Alto, CA, 1975, pp. 293–315.
[46] T.W. Wright, R.C. Batra, The initiation and growth of adiabatic shear band, Int. J. Plast. 1 (1985) 205–212.
[47] T.W. Wright, H. Ockendon, A model for fully formed shear bands, J. Mech. Phys. Solids 40 (1992) 1217–1226.
[48] T.W. Wright, G. Ravichandran, Canonical aspects of adiabatic shear bands, Int. J. Plast. 13 (1997) 309–325.
[49] T.W. Wright, J.W. Walter, On stress collapse in adiabatic shear band, J. Mech. Phys. Solids 35 (1987) 701–720.
[50] C.-S. Yueh, C.-I. Weng, Linear stability analysis of plane couette flow with viscous heating, Phys. Fluids 8 (1996) 1802–1813.
[51] M. Zhou, G. Ravichandran, A.J. Rosakis, Dynamically propagating shear bands in impact-loaded prenotched plates – ii. Numerical simulations, J. Mech. Phys. Solids 44 (1996) 1007–1032.
[52] M. Zhou, A.J. Rosakis, G. Ravichandran, Dynamically propagating shear bands in impact-loaded prenotched plates – i. Experimental investigations of temperature signatures and propagation speed, J. Mech. Phys. Solids 44 (1996) 981–1006.